Author/s:
Crowther, JM;Cross, PJ;Oliver, MR;Leeman, MM;Bartl, AJ;Weatherhead, AW;North, RA;Donovan, KA;Griffin, MDW;Suzuki, H;Hudson, AO;Kasanmascheff, M;Dobson, RCJ

Title:
Structure-function analyses of two plant mesodiaminopimelate decarboxylase isoforms reveal that active-site gating provides stereochemical control

Date:
2019-05-24

Citation:
Crowther, J. M., Cross, P. J., Oliver, M. R., Leeman, M. M., Bartl, A. J., Weatherhead, A. W., North, R. A., Donovan, K. A., Griffin, M. D. W., Suzuki, H., Hudson, A. O., Kasanmascheff, M. & Dobson, R. C. J. (2019). Structure-function analyses of two plant mesodiaminopimelate decarboxylase isoforms reveal that active-site gating provides stereochemical control. Journal of Biological Chemistry, 294 (21), pp.8505-8515. https://doi.org/10.1074/jbc.RA118.006825.

Persistent Link:
https://hdl.handle.net/11343/331887

Structure–function analyses of two plant *meso*-diaminopimelate decarboxylase isoforms reveal that active-site gating provides stereochemical control

Received for publication, November 27, 2018, and in revised form, March 26, 2019 Published, Papers in Press, April 8, 2019, DOI 10.1074/jbc.RA118.006825

Jennifer M. Crowther[‡§], Penelope J. Cross[‡], Michael R. Oliver[§], Mary M. Leeman[¶], Austin J. Bartl[¶], Anthony W. Weatherhead[‡], Rachel A. North[‡], Katherine A. Donovan[‖], Michael D. W. Griffin[‡‡1], Hironori Suzuki[‡], André O. Hudson[¶2], Müge Kasanmascheff[§§3], and Renwick C. J. Dobson[‡ ‡‡4]**

*From the [‡]Biomolecular Interaction Centre and School of Biological Sciences, University of Canterbury, Private Bag 4800, Christchurch 8140, New Zealand, the [§]School of Biological Sciences, University of Edinburgh, Edinburgh EH9 3JG, Scotland, United Kingdom, the [¶]Thomas H. Gosnell School of Life Sciences, Rochester Institute of Technology (RIT), Rochester, New York 14623, the [‖]Department of Cancer Biology, Dana-Farber Cancer Institute, Boston, Massachusetts 02215, the **Department of Biological Chemistry and Molecular Pharmacology, Harvard Medical School, Boston, Massachusetts 02215, the [‡‡]Department of Biochemistry and Molecular Biology, Bio21 Molecular Science and Biotechnology Institute, University of Melbourne, Parkville, Victoria 3010, Australia, and the [§§]Department of Chemistry and Chemical Biology, Technical University of Dortmund, D-44227 Dortmund, Germany*

Edited by Joseph M. Jez

meso*-Diaminopimelate decarboxylase catalyzes the decarboxylation of *meso*-diaminopimelate, the final reaction in the diaminopimelate L-lysine biosynthetic pathway. It is the only known pyridoxal-5-phosphate–dependent decarboxylase that catalyzes the removal of a carboxyl group from a D-stereocenter. Currently, only prokaryotic orthologs have been kinetically and structurally characterized. Here, using complementation and kinetic analyses of enzymes recombinantly expressed in *Escherichia coli*, we have functionally tested two putative eukaryotic *meso*-diaminopimelate decarboxylase isoforms from the plant species *Arabidopsis thaliana*. We confirm they are both functional *meso*-diaminopimelate decarboxylases, although with lower activities than those previously reported for bacterial orthologs. We also report in-depth X-ray crystallographic structural analyses of each isoform at 1.9 and 2.4 Å resolution. We have captured the enzyme structure of one isoform in an asymmetric configuration, with one ligand-bound monomer and the other in an apo-form. Analytical ultracentrifugation and small-angle X-ray scattering solution studies reveal that *A. thaliana* *meso*-diaminopimelate decarboxylase adopts a homodimeric assembly. On the basis of our structural analyses, we suggest a mechanism whereby molecular interactions within the active site transduce conformational changes to the active-site loop. These conformational differences are likely to influence catalytic activity in a way that could allow for D-stereocenter selectivity of the substrate *meso*-diaminopimelate to facilitate the synthesis of L-lysine. In summary, the *A. thaliana* gene loci *At*3g14390 and *At*5g11880 encode functional *meso*-diaminopimelate decarboxylase enzymes whose structures provide clues to the stereochemical control of the decarboxylation reaction catalyzed by these eukaryotic proteins

Stereochemical control of catalysis is a hallmark feature of enzymes. By restricting substrate accessibility and guiding substrate-binding orientation, enzymes precisely dictate substrate specificity and control stereochemistry. For example, in the bacterial type I polyketide synthases, the stereochemical outcome of the native substrate can be predicted simply by the presence of particular sequence motifs within the catalytic domain (1). Similarly, mutation studies have shown that the formation of different stereoisomers by heteroyohimbine synthase appears to be determined solely by a single histidine residue positioned in an active-site loop (2).

In organisms that use the diaminopimelate pathways for the synthesis of lysine, the final step is the decarboxylation of *meso*-diaminopimelate to produce L-lysine and carbon dioxide (3, 4). This reaction is catalyzed by the enzyme *meso*-diaminopimelate decarboxylase (DAPDC).[5] The substrate of the reaction, *meso*-diaminopimelate, features two carboxylate groups

The authors declare that they have no conflicts of interest with the contents of this article. The content is solely the responsibility of the authors and does not necessarily represent the official views of the National Institutes of Health.

This article contains Figs. S1–S3 and supporting Refs. 1–7.

The atomic coordinates and structure factors (codes 6N2A and 6N2F) have been deposited in the Protein Data Bank (http://wwpdb.org/).

[1] Recipient of an Australian Research Council Future Fellowship (Project no. FT140100544.

[2] Supported by National Science Foundation Grant MCB-1120541, National Institutes of Health Grant R15GM120653, and the College of Science and the Thomas H. Gosnell School of Life Sciences at the Rochester Institute of Technology. To whom correspondence may be addressed. Tel.: 585-475-4259; E-mail: aohsbi@rit.edu.

[3] To whom correspondence may be addressed. Tel.: 49-551-201-1379; E-mail: muege.kasanmascheff@tu-dortmund.de.

[4] Supported in part by the New Zealand Royal Society Marsden Fund (Contract UOC1506) and the United States Army Research Laboratory and Army Research Office under Contract/Grant W911NF-11-1-0481. To whom correspondence may be addressed. Tel.: 64-3-369-5145; E-mail: renwick.dobson@canterbury.ac.nz.

[5] The abbreviations used are: DAPDC, *meso*-diaminopimelate decarboxylase; PLP, pyridoxal-5-phosphate; LB, Luria Bertani; IPTG, isopropyl D-1-thiogalactopyranoside; *Sc*-SDH, saccharopine dehydrogenase from *S. cerevisiae*; MurE, *meso*-diaminopimelate ligase; PDB, Protein Data Bank; r.m.s.d., root mean square deviation; SAXS, small-angle X-ray scattering.

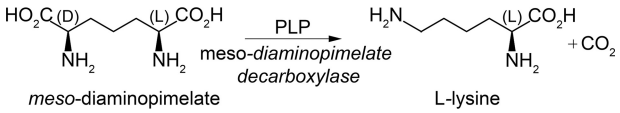

Figure 1. Reaction catalyzed by DAPDC. *meso*-Diaminopimelate contains two stereocenters, D and L. DAPDC removes the carboxylate from the D-stereocenter to produce L-lysine.

located at two different stereocenters: one is an L-stereocenter, and the other is a D-stereocenter. Decarboxylation of *meso*-diaminopimelate specifically at the D-stereocenter results in the production of L-lysine (Fig. 1).

The specificity toward the D-stereocenter of the substrate is a feature unique to DAPDC, as all other pyridoxal-5-phosphate (PLP)–dependent decarboxylases characterized thus far act on L-stereocenters (3). Crystal structures of bacterial DAPDC enzymes reveal that these proteins have an optimal substrate-binding pocket to accommodate the substrate, *meso*-diaminopimelate, and present the D-stereocenter for decarboxylation (5–9). The mechanism by which this stereospecificity is achieved in eukaryotic orthologs remains uncertain.

DAPDC is a member of the alanine racemase family of fold-type III PLP-dependent enzymes. This family also includes the ornithine and arginine decarboxylases (10). Within the active site of these enzymes, the aldehyde moiety of the PLP cofactor is covalently bound to a conserved lysine residue forming a Schiff base (also referred to as an internal aldimine). Upon binding of the substrate, the lysine residue is exchanged for the amino group of the substrate forming an external aldimine. In the reaction catalyzed by DAPDC, the bond between the α-carbon of the external aldimine and the carboxylate group is broken. PLP facilitates the reaction by withdrawing electron density from the substrate through a series of double bonds conjugated to the cationic pyridinium ring, stabilizing the negative charge that develops on the substrate during the reaction (10).

DAPDC is an attractive and putative target for the rational design of herbicides given the fact that the enzyme catalyzes a reaction that is essential for the anabolism of one of the 20 ubiquitous proteogenic amino acids. In addition, it is plausible that herbicides that specifically inhibit DAPDC will not be toxic to humans and animals in general because the DAPDC and lysine anabolic pathways are absent in the animal kingdom.

Our current understanding of the structure and function of DAPDC is largely based on work conducted on archaeal and bacterial orthologs from *Methanococcus jannaschii* (9), *Mycobacterium tuberculosis* (7, 8), *Helicobacter pylori* (5), and *Corynebacterium glutamicum* (6). Previous findings suggest that DAPDC is a dimer in solution, although a tetrameric assembly has been observed in the asymmetric unit of crystal structures of *M. tuberculosis*, and small-angle X-ray scattering data suggest a weak dimer–tetramer equilibrium (8). More recently, solution studies using analytical ultracentrifugation and small-angle X-ray scattering coupled with enzyme kinetics have concluded that DAPDC enzymes from a range of bacterial species form dimers in solution (11). It appears that dimerization is required for catalysis due to the contribution of residues to the active site from both subunits. Consequently, disrupting self-association may provide a means to inhibit these enzymes. Thus far, the only studies that have been reported for a eukaryotic DAPDC are of the two *Arabidopsis thaliana* orthologs that were initially identified and verified through a functional complementation assay (12). Preliminary structural studies have been carried out on these orthologs, but the quaternary association has not yet been investigated (13).

Here, we report the X-ray crystallographic structures of two DAPDC isoforms from the plant species *A. thaliana*, the first in-depth structural characterization of eukaryotic orthologs. Functional complementation studies and kinetic analyses reveal that these isoforms are both authentic DAPDC enzymes, whereas analytical ultracentrifugation and small-angle X-ray scattering solution studies reveal that the protein adopts a homodimeric assembly. We successfully solved the structure of one of the *A. thaliana* isoforms in an asymmetric arrangement, with one active-site loop in the open position and the other closed. These novel observations provide new insight into the catalytic mechanism, giving clues as to how this enzyme exerts stereochemical control of the decarboxylation reaction.

Results and discussion

Complementation analysis of an Escherichia coli lysine auxotrophic mutant demonstrates that At-DAPDC1 and At-DAPDC2 can rescue endogenous lysine biosynthesis

To assess whether the identified genes annotated by the locus tags *At*3g14390 and *At*5g11880 are functional DAPDC enzymes, complementation analyses were conducted. The *E. coli* CGSC strain 10193 harbors a mutation in the gene that encodes for DAPDC (*lysA*). This mutation results in a lysine auxotrophic phenotype where the mutant is able to grow only in the presence of exogenous lysine. As such, we can test the functionality of *At*-DAPDC enzymes by whether or not they can functionally complement the *lysA* mutant. It should be noted that previous work by our group shows that both *At*-DAPDC isoforms were able to complement another *lysA* mutant in a study that surveyed the lysine anabolic genes from *A. thaliana* (12). However, the previous analysis used full-length cDNAs for both proteins, although the analysis reported here was completed without the sequences that encode the predicted transit peptide that denotes localization to the chloroplast (13).

To ascertain whether the genes of interest are able to complement the *E. coli lysA* mutation, mutants were transformed with an empty vector (pBAD33) or with pBAD33 expressing *At*-DAPDC1 or *At*-DAPDC2. The plasmid pBAD33 possesses a promoter that is inducible in the presence of arabinose and repressible in the presence of glucose (14). Surprisingly, both *At*-DAPDC enzymes were only able to rescue the mutant when their expression was repressed by glucose (Fig. 2). It is believed that under this condition there is still enough basal expression to allow for the synthesis of adequate quantities of lysine for protein synthesis to facilitate growth.

Conversely, in cells in which the expression of *At*-DAPDC is enhanced (in the presence of arabinose), no growth was seen (Fig. 2). Rather than this being due to a lack of lysine production to facilitate protein synthesis, we propose that this result is due to the depletion of *meso*-diaminopimelate, the substrate of DAPDC. In Gram-negative bacteria, such as *E. coli*, *meso*-di-

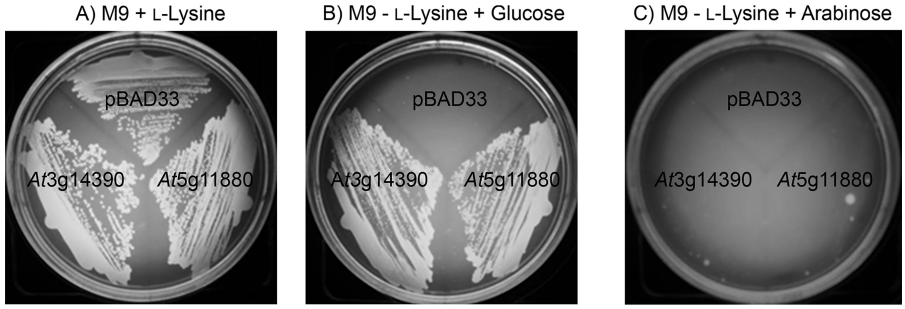

Figure 2. Functional complementation analysis of an *E. coli lysA* mutant (CGSC strain 10193) using *At*-DAPDC1 and *At*-DAPDC2. Colonies were replica-plated on media with lysine (*A*) or without lysine, supplemented with glucose (*B*) or arabinose (*C*).

aminopimelate is used as the cross-linking amino acid in the peptide stem of peptidoglycan, a process facilitated by *meso*-diaminopimelate ligase (MurE) (15). Therefore, the induced expression of *At*-DAPDC enzymes in lysine-free media leads to cell death because the native MurE cannot compete with the overexpressed DAPDC, and thus, although the organism is able to synthesize L-lysine, it has impaired peptidoglycan synthesis. Nonetheless, these results indicate that the two genes encode authentic DAPDC enzymes and are able to function in *E. coli* without the predicted chloroplast transit peptide sequences.

Recombinant At-DAPDC1 and At-DAPDC2 are both enzymatically active

Although both enzymes are active, their rate of turnover is surprisingly low. The catalytic activities of recombinant *At*-DAPDC1 and *At*-DAPDC2 were examined using the DAPDC–SDH-coupled assay (16). We first determined that the rate of catalysis was linear across an enzyme concentration range of 0 – 800 nM (Fig. 3*A*). We therefore chose to collect the initial rate data at an enzyme concentration of 550 nM. The initial rate data for both enzymes fitted well to the Michaelis-Menten equation (Fig. 3, *B* and *C*). The purified *At*-DAPDC enzymes are both catalytically active with apparent K_m values of 5.1 and 4.8 mM, V_{max} values of 85 and 229 nmol min^{-1}, and catalytic rate constants (k_{cat}) of 0.005 and 0.014 s^{-1}, for *At*-DAPDC1 and *At*-DAPDC2, respectively (Table 1). The K_m values are consistent with other previously characterized DAPDC enzymes (0.68 mM (*Bacillus anthracis*), 0.97 mM (*E. coli*), 1.6 mM (*M. tuberculosis*), and 1.9 mM (*Vibrio cholerae*) (11)). In contrast, the catalytic rate constants for the *A. thaliana* DAPDC orthologs are much lower than their bacterial counterparts (58 s^{-1} (*B. anthracis*), 55 s^{-1} (*E. coli*), 28 s^{-1} (*M. tuberculosis*), and 22 s^{-1} (*V. cholerae*) (11)). This may be a reflection of the lower temperatures used here (30 °C, compared with 37 °C). Peverelli *et al.* (11) found that dimerization of DAPDC was required for catalysis, given that residues are required from each subunit to form the active site. Therefore, we sought to investigate the quaternary structure of the recombinant *At*-DAPDC enzymes in solution.

At-DAPDC enzymes exist in a monomer– dimer equilibrium

Although monomeric (5, 17), dimeric (6, 7, 9), and tetrameric (8) assemblies have been observed in crystal structures of prokaryotic orthologs of DAPDC, the quaternary structure has not yet been investigated for any plant orthologs. To address this, the quaternary structure of the two *At*-DAPDC enzymes were characterized by analytical ultracentrifugation. Sedimentation velocity data were fitted to continuous size distribution models yielding *c*(*s*) distributions (Fig. 4). For both proteins (at concentrations between 5 and 20 μM), two species with sedimentation coefficients of around 3.5 and 5 S are evident in solution. When fitted to a continuous mass distribution model, the estimated masses of each species are ~50 and ~100 kDa (based on frictional ratios of 1.51 for *At*-DAPDC1 and 1.43 for *At*-DAPDC2, calculated during the *c*(*s*) analyses); therefore, these peaks correspond to a monomer and dimer (given the theoretical monomeric molecular masses of 53,807 Da for *At*-DAPDC1 and 54,240 Da for *At*-DAPDC2).

The plots in Fig. 4, *A* and *B,* have been normalized to the height of the peak corresponding to the dimer, revealing that with increasing protein concentrations the proportion of protein found in the dimeric form increases. This indicates that the protein is in a concentration-dependent monomer– dimer self-association. The sedimentation velocity data were further analyzed using the advanced van-Holde/Weischet method. This method is model-independent and directly assesses the shape of the sedimenting boundary to provide an estimate of the proportion of each species in solution (Fig. 4, *C* and *D*). The half-parabolic shape of the van-Holde/Weischet plots are characteristic of mass action and support the conclusion that this protein exists in equilibrium between its monomeric and dimeric forms.

The predominant species at these concentrations is the dimer, suggesting that the dimer dissociation constants (K_D^{2-1}) for these enzymes are below the concentrations examined here. Sedimentation velocity data at the lowest concentration (5 μM) were fitted to a monomer– dimer model. These analyses estimate the K_D^{2-1} values for both *At*-DAPDC enzymes to be less than 1 μM (Table 2). The enzyme assays were conducted at a concentration of 550 nM; thus, there is likely a mixture of monomers and dimer in solution at this concentration. However, because the rate *versus* enzyme concentration (Fig. 3*A*) is linear from 200 to 800 nM, which spans the estimated K_D^{2-1} for both enzymes (~650 nM), either both the monomer and dimer are similarly active or the presence of substrates lowers the dissociation constant, resulting in a predominantly dimeric species at the concentration used to collect the initial rate data. Given the results of Peverelli *et al.* (11), where mutants that disrupt the dimer interface of *V. cholerae* DAPDC have attenuated activity, we suggest that the latter is a more reasonable explanation of the data.

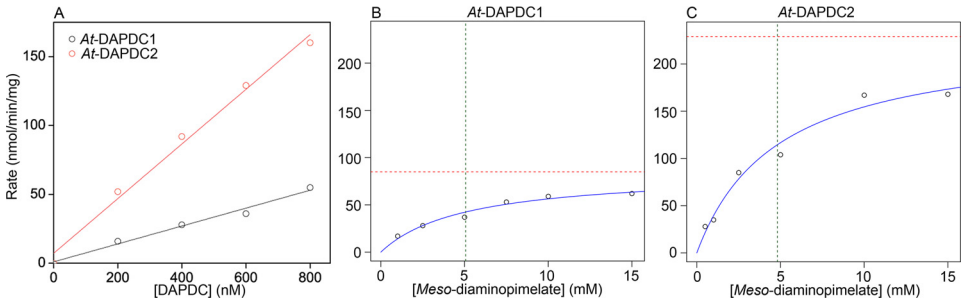

Figure 3. Enzyme kinetic analysis of *At*-DAPDC1 and *At*-DAPDC2. The catalytic activity was assessed using the DAPDC–SDH-coupled assay (19). *A,* rate of reaction relative to enzyme concentration shows the expected linear response between 200 and 800 nM for both *At*-DAPDC1 and *At*-DAPDC2. Given this plot, the concentration of enzyme used for the initial rate experiments (*B* and *C*) was 550 nM, because this was in the linear range. *B* and *C,* data (*circles*) represent the activity of *At*-DAPDC as a function of substrate (*meso*-diaminopimelate) concentration, fitted to the Michaelis-Menten equation (*solid line*). The R^2 for the fit to *At*-DAPDC1 initial rate data was 97%, and the fit to the *At*-DAPDC2 initial rate data was 98%. The *green dashed lines* indicate K_m values, and the *red dashed lines* indicate V_{max}.

Table 1
Kinetic parameters of *At*-DAPDC1 and *At*-DAPDC2

	K_m	V_{max}	k_{cat}	R^2
	mM	*nmol·min − 1*	*s − 1*	
At-DAPDC1	5.1 (2.5–10.6)	85 (66–118)	0.005	0.97
At-DAPDC2	4.8 (2.4–10.5)	229 (177–323)	0.014	0.98

Structural characterization of At-DAPDC enzymes

At-DAPDC1 and *At*-DAPDC2 were crystallized as reported previously (13). All relevant data-collection and processing parameters are given in Table 3. Globally, the structures of the two *At*-DAPDC enzymes show considerable similarity to each other and to previously characterized bacterial DAPDC enzymes (Fig. S1) (5–9). For both structures, the asymmetric unit is a dimer (Fig. 5*A*), with each monomer composed of two domains: an alanine racemase-like fold and an $(\alpha/\beta)_8$ barrel domain (Fig. 5*B*). The alanine racemase-like domain (shown in *yellow*, Fig. 5*B*) is composed of interlocking β-strands from both the N and C termini (residues 1–50 and 301–440, amino acid numbering corresponding to that of *At*-DAPDC1). The $(\alpha/\beta)_8$ barrel domain (residues 51–300, shown in *red* in Fig. 5*B*) contains the active site at its core and features an extended active-site loop between the fifth β-sheet (β5) and sixth α-helix (α6) of the barrel (residues 165–194). The monomers associate in a head–to–tail arrangement to form a dimer, with the two active sites located at the dimer interface.

To validate that the dimeric assembly observed in the crystal structures is an accurate representation of the protein structures in solution, small-angle X-ray scattering experiments were conducted. The structural parameters obtained from these analyses are summarized in Table 4. The maximum dimensions of the particles (105 and 113 Å for *At*-DAPDC1 and *At*-DAPDC2) and estimated molecular masses (95 and 94 kDa) are most consistent with that of a dimer (given the theoretical dimeric molecular masses of 107 and 108 kDa for *At*-DAPDC1 and *At*-DAPDC2). Furthermore, theoretical scattering curves were generated based on the crystal structures of *At*-DAPDC for both a monomer and a dimer. The experimental scattering obtained for samples of *At*-DAPDC in solution are a much closer fit to the scattering calculated for a dimer than for a monomer (χ^2 = 0.41 and 0.71, compared with 3.26 and 8.09), suggesting that the dimeric quaternary arrangements observed in the crystal structures are correct (Fig. 5, *C* and *D*).

Active sites of At-DAPDC enzymes are similar to prokaryotic orthologs of DAPDC

In the structure of *At*-DAPDC1, electron density consistent with the structure of a PLP molecule can be observed in both active sites (Fig. 6*A*). The density is continuous with a free lysine molecule, probably resulting from the supplementation of free lysine in the crystallization conditions. This external aldimine is likely to closely reflect the catalytic intermediate formed between *meso*-diaminopimelate and PLP during the decarboxylation reaction (5). PLP is positioned near a conserved lysine residue (Lys-77) that likely forms the internal aldimine with PLP when no substrate is present. In contrast, in the structure of *At*-DAPDC2, electron density attributable to PLP and a molecule of free lysine is visible in one active site only (Fig. 6*B*). No such electron density is observed in the other active site.

The same interactions are present in the PLP-bound active sites of *At*-DAPDC1 and *At*-DAPDC2 (see LigPlot in Fig. S2). For the following analyses, residue numbering according to *At*-DAPDC2 is used, to allow for comparisons to be made between the ligand-bound and apo monomers. PLP forms hydrogen bonds directly with Ser^{223}, Arg^{299}, Tyr^{396}, Gly^{298}, Gly^{260}, and Glu^{296} and via water molecules with Leu^{261}, Arg^{299}, Ser^{300}, Arg^{169}, and Cys^{367*} (the asterisk denotes that this residue is contributed from the opposing monomer) (Fig. 6*C*). His^{220} is positioned parallel to PLP, ~3.5 Å above the aromatic ring of the cofactor, appropriately positioned to facilitate a π-stacking interaction (Fig. 6*C*). The supplemented lysine molecule forms hydrogen bonds with Arg^{299}, Arg^{335}, Tyr^{339}, and Glu^{368*} (Fig. 6*D*).

The active-site architecture described here for the *A. thaliana* orthologs of DAPDC is similar to that observed in previously characterized bacterial orthologs (5–9), suggesting that eukaryotic DAPDC enzymes employ the same methods to direct stereochemical control. This includes anchoring of the L-stereocenter of *meso*-diaminopimelate presenting the D-stereocenter for catalysis, facilitated by the conserved residues Arg^{299}, Arg^{335}, Tyr^{339}, and Glu^{368*} (see Fig. S3 for sequence alignment). This also includes the contribution of residues from both subunits toward the active site, suggesting that, as in bacterial orthologs (11), the dimer is the catalytically active form.

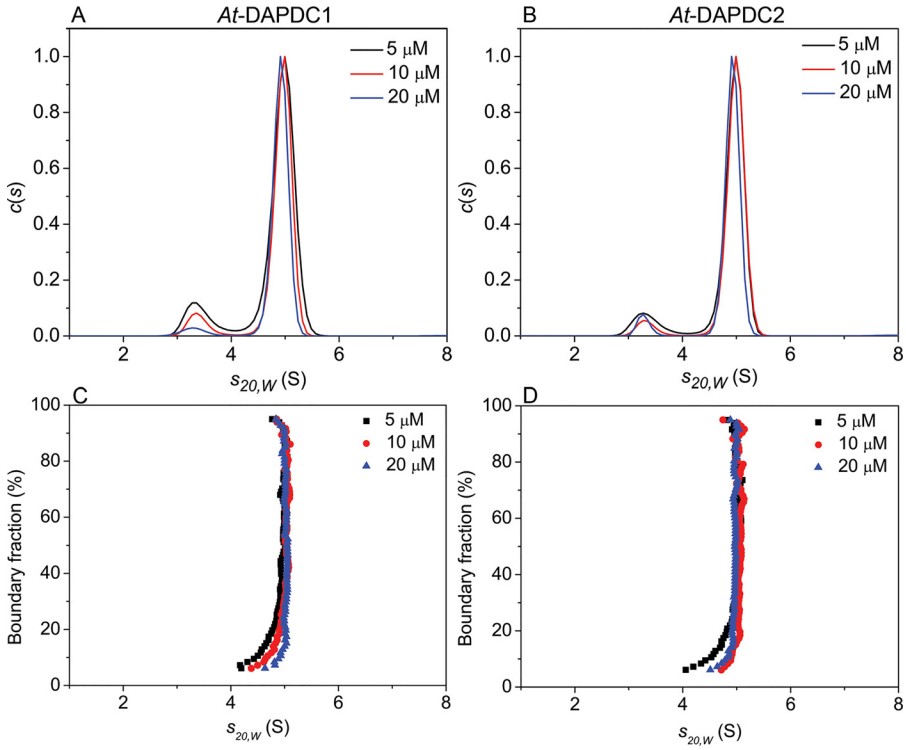

Figure 4. Sedimentation velocity analysis of *At*-DAPDC1 and *At*-DAPDC2. Continuous sedimentation coefficient ($s_{20,w}$) distributions for *At*-DAPDC1 (*A*) and *At*-DAPDC2 (*B*) at 5 μM (*black line*), 10 μM (*red line*), and 20 μM (*blue line*) are shown. Enhanced van-Holde/Weischet analyses for *At*-DAPDC1 (*C*) and *At*-DAPDC2 (*D*) at 5 μM (*black squares*), 10 μM (*red circles*), and 20 μM (*blue triangles*) are shown.

Table 2

Sedimentation velocity-fitting results for *At*-DAPDC1 and *At*-DAPDC2 to a reversible monomer–dimer equilibrium model

Values in parentheses represent 95% confidence intervals determined by conducting 96 Monte Carlo iterations. The r.m.s.d. for the fits were 0.0043 and 0.0045.

	At-DAPDC1		*At*-DAPDC2	
	Monomer	Dimer	Monomer	Dimer
Molecular mass (Da)[a]	53,807	107,614	54,240	108,480
Sedimentation coefficient (*s*)	3.65 (3.62–3.68)	5.11 (5.10–5.13)	3.30 (3.16–3.44)	5.21 (5.20–5.22)
Frictional ratio (f/f_0)	1.20 (1.15–1.24)	1.36 (1.31–1.40)	1.48 (1.42–1.54)	1.49 (1.47–1.51)
Dimer dissociation constant (K_D^{2-1}) μM	0.66 (0.56–0.76)		0.63 (0.53–0.74)	

[a] Molecular mass was estimated from the protein sequence in UltraScan.

Conformational differences between the apo and PLP-bound monomers of At-DAPDC2 provide insight into stereochemical control

The PLP-bound monomer of *At*-DAPDC2 shows distinct conformational differences to the apo monomer (without PLP and lysine). When superimposed, the r.m.s.d. value is 0.456, compared with 0.128 when aligning the two monomers of *At*-DAPDC1 (both PLP-bound). This is the first time an asymmetric dimer has been observed in a structure of DAPDC and may give further insight into the stereochemical control of the decarboxylation reaction mediated by DAPDC.

One such conformational difference between the apo and PLP-bound forms is the position of the active-site loop. The active-site loop is the region between Arg^{169} and Lys^{197} (numbering according to *At*-DAPDC2) that extends past the entrance to the active site (Fig. 7). The electron density of this region is often poorly defined in structures of DAPDC (5), because of the flexibility of this loop. Similarly, density was absent and could not be modeled for sections of the active-site loop in chain B of *At*-DAPDC1 (residues 170–180, *green loop* in Fig. 7*A*) and chain A of *At*-DAPDC2 (residues 180–188, *blue loop* in Fig. 7*B*). By comparing the positions of residues at each end of the loop (for which there is clear density), a significant change in the position of the loop becomes apparent between the apo and PLP-bound forms of *At*-DAPDC2 (Fig. 7*B*). The loop is in an open conformation in the apo-form, whereas it is closed in the PLP-bound form. This can be seen most clearly when observing residue Phe^{191}; in the PLP-bound monomer (*green loop*) this phenylalanine residue lies near the edge of the active site (shown by the *purple* PLP molecule) (Fig. 7*B*). Conversely, in the apo monomer (*blue loop*), Phe^{191} is shifted by 19 Å and is buried in the interface between the α7 and α8 helices of the $(\alpha/\beta)_8$ barrel (Fig. 7*B*). Interestingly, judging by the position of this phenylalanine residue, all structures of DAPDC orthologs currently deposited in the PDB appear to have loops in the closed conformation.

In the active site of the apo monomer of *At*-DAPDC2, several differences can be observed compared with the PLP-bound active site. Most of these involve reorientations of side chains that are no longer bound by hydrogen bonds to either PLP or lysine. However, some residues undergo more significant conformational change, including Arg^{169}, His^{218}, and His^{220}

Table 3
Processing and refinement parameters
Values in parentheses pertain to the shell of highest resolution.

	At-DAPDC1	*At*-DAPDC2
Processing statistics		
Space group	$P2_12_12$	$P2_1$
Unit cell parameters, *a*, *b*, *c* (Å); β (°)	80.9, 121.5, 88.6; 90.0	51.3, 107.9, 80.3; 98.1
Resolution range (Å)	42.62–1.88 (1.92–1.88)	39.77–2.35 (2.43–2.35)
No. of measurements	525,698 (31,362)	132,573 (11,672)
No. of unique reflections	71,841 (4528)	35,978 (3454)
Redundancy	7.3	3.7
Completeness (%)	99.9 (98.7)	99.7 (97.9)
$I/\sigma(I)$	9.6 (1.5)	5.5 (1.3)
$CC_{½}$	0.997 (0.678)	0.987 (0.694)
R_{merge}	0.138 (1.197)	0.167 (0.824)
Wilson *B* value (Å^2)	22.2	34.0
Refinement statistics		
Resolution (Å)	1.88	2.35
R_{work}	0.17	0.20
R_{free}	0.21	0.27
No. of amino acid residues	436	440
No. of water molecules	696	311
No. of others	4	2
Mean refined B (Å^2)		
Protein	26.42	32.6
Ligands	16.99	33.77
Waters	35.02	28.59
r.m.s.d. from target values		
Bond lengths (Å)	0.71	0.71
Bond angles (°)	0.84	0.84
Ramachandran		
Most favored (%)	96.7	95.8
Allowed (%)	3.0	4.1
Disallowed (%)	0.2	0.1
PDB codes	6N2A	6N2F

(Fig. 7*C*). In the apo-form, Arg^{169} exists in a twisted conformation, forming a hydrogen bond with Asp^{145}. His^{218} and His^{220} are located in close proximity facing toward Arg^{169}. In the PLP-bound form, His^{220} is reoriented to form a π-stacking interaction with PLP, whereas His^{218} fills the space vacated by His^{220}. Arg^{169} adopts an extended conformation running parallel to His^{220} and His^{218} that is stabilized through a hydrogen bond with the backbone carbonyl of His^{220}. This constitutes a 2.5 Å movement of the Cα atom of Arg^{169}. Arg^{169} is the first residue of the active-site loop, and thus it is conceivable that this conformational rearrangement may be associated with repositioning of the active-site loop into the closed configuration.

Closure of the active-site loop has been shown to enhance the rate of catalysis in DAPDC from *H. pylori* (5). As well as stabilizing the catalytic intermediate, closure of the active-site loop may be important in excluding other molecules from entering the active site, preventing side reactions, or excluding water from the active site during the reaction; in so doing, this may enhance catalysis as production of the nonpolar product, CO_2, would be expected to occur faster in a nonpolar environment than surrounded by water.

When *meso*-diaminopimelate is modeled in the active site of *At*-DAPDC2 in the same configuration as L-lysine (shown in *yellow* in Fig. 7*D*), the D-stereocenter carboxyl can be suitably accommodated within the active site, whereas steric hindrance (with Cys^{367} and Glu^{368}) would prevent binding in the reverse orientation. In this configuration, we can also see a possible hydrogen bond between the substrate and His^{220} (within 3 Å of each other). It is possible, therefore, that approach of the substrate is able to stabilize the position of His^{220} over the pyridoxal ring and subsequently encourage the closure of the active-site loop, but this would occur only when the D-stereocenter is oriented for decarboxylation, not the L-stereocenter. If active-site loop closure is required to enhance catalysis in *At*-DAPDC, as it does in *H. pylori* (5), this may provide an extra means by which DAPDC exerts stereochemical control over the decarboxylation of *meso*-diaminopimelate.

Conclusion

We have established that the *A. thaliana* gene loci, *At*3g14390 and *At*5g11880, encode functional DAPDC enzymes. The recombinantly expressed eukaryotic enzymes are catalytically active but exhibit much lower activity than previously characterized bacterial orthologs. To determine whether this is a feature of plant DAPDC enzymes will require further characterization of eukaryotic DAPDC orthologs. Solution studies reveal that both *At*-DAPDC enzymes exist in a monomer–dimer equilibrium in solution; however, the dimer is likely the catalytically active form due to the requirement of residues from each subunit to form the active site. This is in line with previously characterized bacterial orthologs of DAPDC.

The crystal structures of the *At*-DAPDC enzymes reveal that the eukaryotic orthologs characterized here for the first time are very similar structurally, including the active-site architecture, to the prokaryotic forms of DAPDC previously characterized. The fortuitous capture of *At*-DAPDC2 in an asymmetric dimer, with one monomer in the apo-form and the other in a ligand-bound form, provides valuable insight into the conformational transition that occurs upon PLP binding. Furthermore, this is the first DAPDC structure that has the active-site loop in an open conformation.

Based on our structural data, we propose that the following conformational changes are important for catalysis and stereochemical selection of the substrate. First, binding of PLP initiates rearrangements within the active site, specifically the reorientation of Arg^{169}, His^{218}, and His^{220}. These conformational changes are propagated to the active-site loop, through Arg^{169} which is a part of this loop; the position of the active-site loop is known to influence the catalytic activity of DAPDC enzymes (5). Second, we have shown that the substrate, *meso*-diaminopimelate, is positioned through interactions with conserved active-site residues to form an additional hydrogen bond to His^{220}. This further stabilizes the closed active-site loop conformation, mediated through Arg^{169}, and can only occur when the D-stereocenter is oriented for decarboxylation. These findings provide further clues into how DAPDC targets the D-stereocenter of the substrate, *meso*-diaminopimelate, for decarboxylation during catalysis—knowledge that is necessary to assist in the design of effective inhibitors that may act as herbicides or antibiotics.

Experimental procedures

Cloning of the cDNAs annotated by the locus tags At3g14390 and At5g11880

The cDNAs *At*3g14390 (*At*-DAPDC1) and *At*5g11880 (*At*-DAPDC2), encoding the two isoforms of DAPDC from *A. thaliana*, were cloned as described previously (13). The forward and reverse primers used to amplify the *At*3g14390 cDNA were 5′-CCCCCGGATCC**ATG**GCCGCCGTCGTTTCTCAAAACTCGTCC-3′ and 5′-CCCCCGTCGAC**TCA**TAGACCTTC-

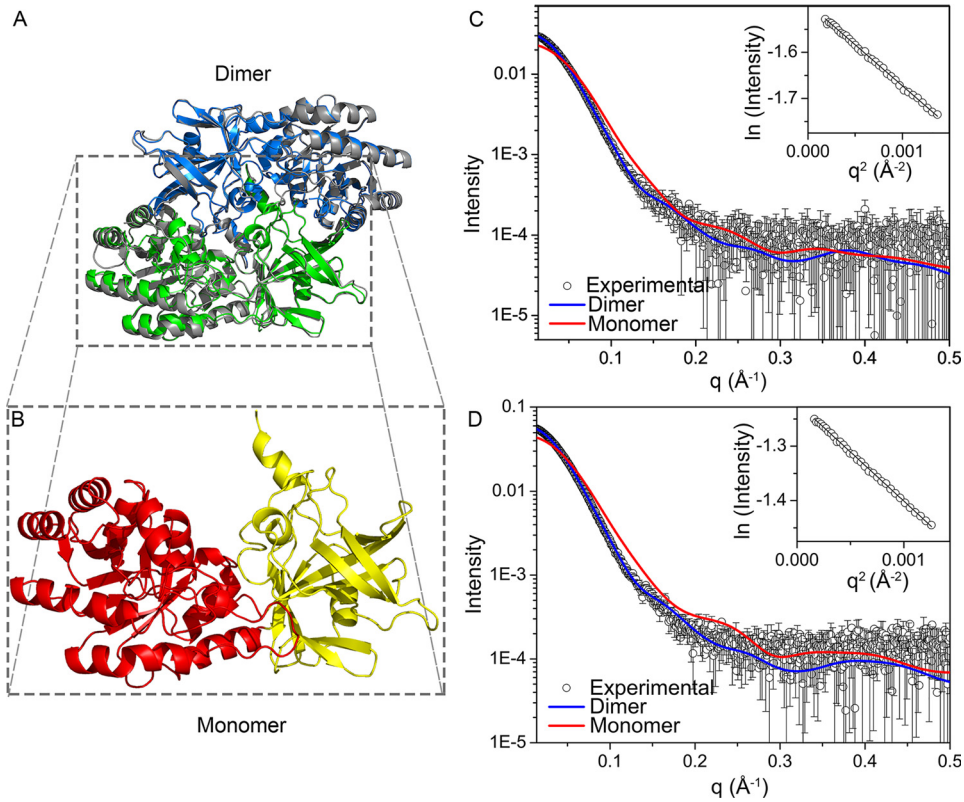

Figure 5. *A*, crystal structure of dimers of *At*-DAPDC1 (*gray*, PDB code 6N2A) and *At*-DAPDC2 (separate chains colored in *blue* and *green*, PDB code 6N2F). *B*, monomer of *At*-DAPDC1: the alanine racemase-like domain is colored in *yellow*, and the $(\alpha/\beta)_8$ barrel domain is colored in *red*. Small-angle X-ray scattering profile of *At*-DAPDC1 (*C*) and *At*-DAPDC2 (*D*) in solution was compared with the theoretical scattering calculated based on the crystal structure of a monomer and a dimer of each protein.

Table 4
Small-angle X-ray scattering structural parameters.

	At-DAPDC1	*At*-DAPDC2
$I(0)$ (cm^{-1}) (from Guinier)	0.0320 ± 0.0001	0.0600 ± 0.0001
Guinier $R_g/I(0)$	34.74 ± 0.03	35.59 ± 0.06
$P(r)$ $R_g/I(0)$	34.77 ± 0.03	35.64 ± 0.06
D_{max} (Å)	105	113
Porod volume (Å^3)	161,000	160,000
Molecular mass determination (kDa) (from Porod volume)	94,706	94,118
Calculated dimer molecular mass from sequence (kDa)	107,608	108,480

AAAGAAACGCAAATGGTC-3′. The forward and reverse primers used to amplify the *At*5g11880 cDNA were 5′-CCCC-CGGATCC**ATG**GCCGCCGTTTCCCAAAACTCCTACCA-AA-3′ and 5′-CCCCCGTCGAC**TCA**TAGTCCTTCAAAGA-AACGTAAATGGTC-3′. The underlined nucleotides represent the restriction enzyme sites used in the cloning of the cDNAs, and the bold italicized nucleotides represent initiation and termination codons. The PCR protocols were designed to exclude the first 144 and 147 nucleotides from the *At*3g14390 and *At*5g11880 cDNAs, respectively, as these nucleotides encode a predicted transit peptide that allows localization to the chloroplast. The truncated cDNAs were cloned between the BamHI and SalI restriction sites of pET30A to produce the plasmids pET30a::*At*3g14390 and pET30a::*At*5g11880. The constructs have the following amino acid residues (MHHHHHHSSGLVPRGSGMKETAAAKFDRQHM-DSPDLGTDDDDKAMADI) at the N-terminal end of each recombinant enzyme, yielding polypeptides of 53,807 Da (*At*-DAPDC1) and 54,240 Da (*At*-DAPDC2).

Functional complementation

The plasmids used for functional complementation were produced by subcloning the XbaI and SalI fragment from pET30a::*At*3g14390 and pET30a::*At*5g11880 into pBAD33 (14) to produce the plasmids pBAD33::*At*3g14390 and pBAD33::*At*5g11880. The proteins produced from the pBAD33 constructs are identical to the proteins produced from the pET30a constructs.

An *E. coli* lysine auxotrophic mutant (CGSC strain 10193: (Δ*(araD–araB) 567*, Δ*lacZ4787* (*::rrnB-3*), λ$^-$,Δ*lysA763::kan, rph-1,* Δ(*rhaD–rhaB*) *568, hsdR514*) (18)) was transformed with either the empty pBAD33 vector, pBAD33::*At*3g14390 or pBAD33::*At*5g11880. Colonies were selected on Luria-Bertani (LB) agar plates supplemented with 34 μg ml^{-1} chloramphenicol and 50 μg ml^{-1} kanamycin. Individual colonies were then replica-plated onto M9 medium supplemented with 0.5% (w/v) glycerol, with or without 50 μg ml^{-1} lysine, and 0.2% (w/v) arabinose or glucose. The colonies were incubated at 30 °C for 48 h.

Protein expression and purification of At-DAPDC for structural characterization

The expression vectors pET30a::*At*3g14390 and pET30a::*At*5g11880 were transformed into *E. coli* Rosetta (DE3) cells. The transformed cells were grown in LB medium (with 50 μg ml^{-1} kanamycin and 34 μg ml^{-1} chloramphenicol) at 37 °C until the A_{600} reached ~0.5. Expression at 26 °C overnight was

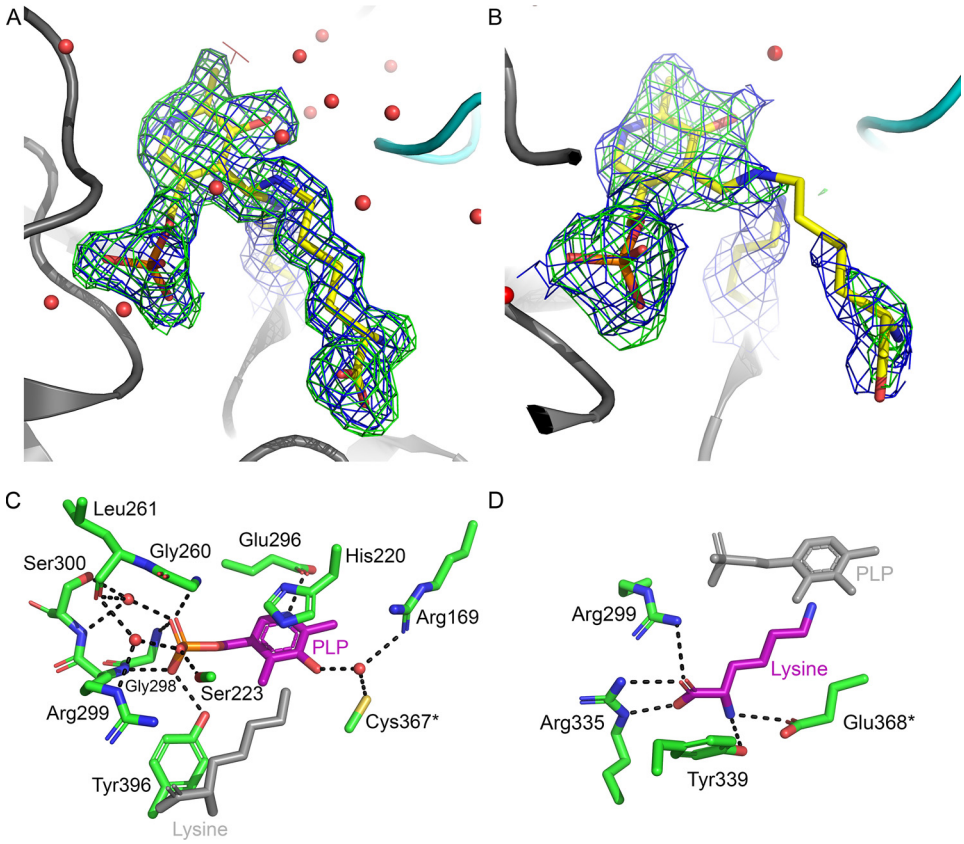

Figure 6. Omit maps for the active site of *At*-DAPDC1 (active site shown is representative of both active sites (*A*), and the PLP/lysine-bound *At*-DAPDC2 active sites (*B*) are shown. $F_o - F_c$ electron density map shown in *blue*, contoured at 1.0 σ, and the $2F_o - F_c$ map is shown in *red* and *green* to indicate negative and positive electron density, contoured at 3.0 σ. PLP, free lysine, Lys-77 (*At*-DAPDC1), and Lys-81 residue (*At*-DAPDC2) are shown as *yellow sticks*, and the rest of the protein is shown in *cartoon* form with one chain colored *gray* and the other chain colored *cyan*. PLP- (*C*) and lysine (*D*)-binding residues for *At*-DAPDC2 are shown.

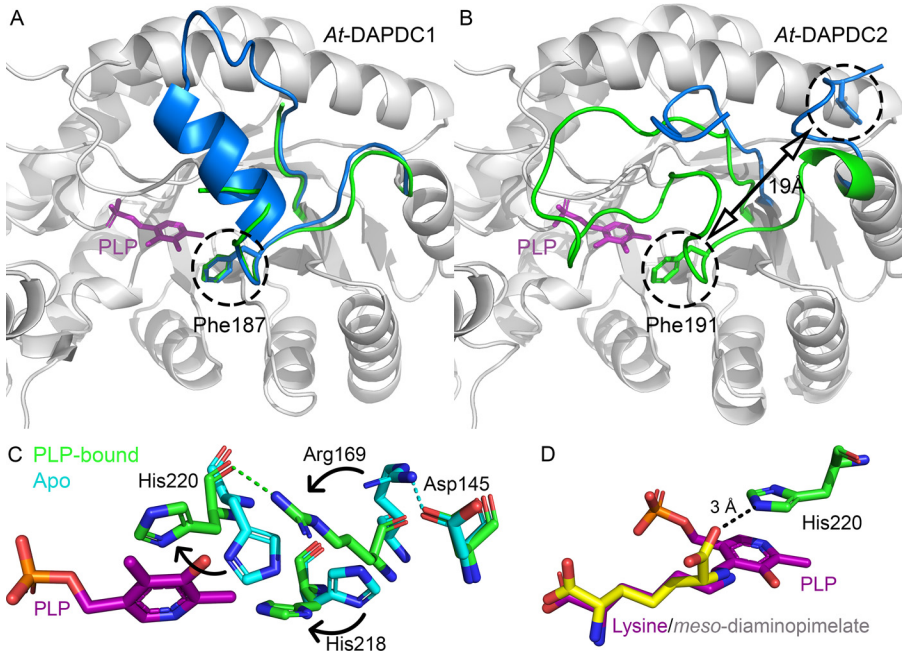

Figure 7. Active-site loop of *At*-DAPDC1 (*A*) and At-DAPDC2 (*B*) is shown. PLP molecule is shown in *purple* to indicate the location of the active site. In both monomers of *At*-DAPDC1, the active-site loop is closed over the active site. In the apo monomer of *At*-DAPDC2 (shown in *blue*), the active-site loop is in an open conformation. *C,* conformational changes in the active site between the PLP-bound (*green sticks*) and apo (*blue sticks*) monomers of *At*-DAPDC2. *D,* when *meso*-diaminopimelate is modeled in the same position as L-lysine, the carboxylate of the D-stereocenter is positioned close enough to form a hydrogen bond with residue His-220.

induced by addition of 0.5 mM isopropyl D-1-thiogalactopyranoside (IPTG).

The cell pellet was resuspended in buffer (50 mM sodium phosphate, 300 mM sodium chloride, 10 mM imidazole, pH 8.0) and lysed by sonication using a cell disruptor (Vibra-Cell VC 750; Sonics). The lysate was clarified by centrifugation (12,000 × *g*, 4 °C, 10 min) and loaded onto a His-Trap FF Crude 5-ml column (GE Healthcare). The bound His-tagged protein was eluted with increasing imidazole concentrations up to 250 mM. Fractions containing protein were pooled and concentrated to 3 ml using a 30-kDa molecular mass cutoff spin concentrator (Vivaspin centrifugal concentrator, Sartorius). The concentrated solution was further purified on a HiLoad 10/30 Superdex 200 column (GE Healthcare) pre-equilibrated with buffer (20 mM Tris, 100 mM sodium chloride, pH 8.0). All purification steps were carried out at 4 °C. Peak fractions were concentrated to 10 mg ml^{-1} using a 30-kDa molecular mass cutoff spin concentrator. Protein concentrations were determined spectrophotometrically using the extinction coefficient at 280 nm of 33,350 M^{-1} cm^{-1}, calculated from amino acid sequences using ExPASy ProtParam (19), and Beer's law (20).

Protein expression and purification of At-DAPDC and Sc-SDH for enzymatic assays

pET30a::*At*3g14390, pET30a::*At*5g11880 and pET16b::*Sc*Lys1 (expressing saccharopine dehydrogenase from *Saccharomyces cerevisiae*) were transformed into *E. coli* BL21-CodonPlus-RIPL strain (Agilent Technologies). Cells were grown in LB media containing 50 μg ml^{-1} kanamycin and 34 μg ml^{-1} chloramphenicol (*At*-DAPDC) or 50 μg ml^{-1} ampicillin and 34 μg ml^{-1} chloramphenicol (*Sc*-SDH) at 37 °C, to an A_{600} of 0.5. Protein expression was induced with 1.0 mM IPTG for 24 h at 18 °C. The cells were lysed by sonication in a solution of 50 mM sodium phosphate, pH 8.0, and 300 mM sodium chloride. The extract was incubated with Talon Metal Affinity Resin (Clontech) for 30 min at 4 °C. The resin was washed five times with sonication buffer containing 10 mM imidazole, pH 8.0, and the enzyme was eluted with buffer containing 250 mM imidazole. The pure protein was concentrated in an Amicon Ultra 10,000 molecular weight cutoff spin concentrator replacing the elution buffer with 100 mM Tris containing 1 mM DTT and 2 mM EDTA, pH 8.0. Protein concentration was determined by the Bradford assay (21).

DAPDC kinetic assay

A coupled assay, using *Sc*-SDH as the coupling enzyme, was used to measure the activity of *At*-DAPDC1 and *At*-DAPDC2 (16). L-Lysine produced from *meso*-diaminopimelate by DAPDC is used as the substrate of *Sc*-SDH along with α-ketoglutarate and NADH. The oxidation of NADH to NAD^+ can be monitored spectrophotometrically as a decrease in the absorbance at 340 nm over time.

Titration assays varying the concentration of substrate, *meso*-diaminopimelate, were buffered with 100 mM Tris, pH 8.0, using a final assay concentration of 200 μM NADH, 25 mM α-ketoglutarate, and an excess of *Sc*-SDH (40 μg). With a final reaction volume of 500 μl, *meso*-diaminopimelate was added to various final concentrations ranging from 0 to 15 mM. Reactions were initiated with the addition of either *At*-DAPDC1 or *At*-DAPDC2 to a final concentration of 550 nM. All coupled assays were performed at 30 °C, and absorbance at 340 nm was measured as a function of time. Data were analyzed using a Michaelis-Menten kinetic model to determine the V_{max}, K_m, and k_{cat} values.

Analytical ultracentrifugation

Sedimentation velocity experiments were performed in a Beckman Coulter XL-I analytical ultracentrifuge. Sedimentation was monitored using the absorbance optical system. *At*-DAPDC1 and *At*-DAPDC2 were analyzed at three protein concentrations: 5, 10, and 20 μM in 20 mM Tris, 150 mM sodium chloride at pH 8.0. Sample solutions were loaded into 12-mm double-sector quartz cells and centrifuged at 50,000 rpm at 20 °C. Intensity data were recorded over a radial position range of 6.0 to 7.25 cm, with a step size of 0.003 cm. Different wavelengths were monitored depending on the protein concentration; 281 nm was used for 20 μM samples, and lower concentrations were analyzed at 236 nm.

The sedimentation data were fitted to a continuous size–distribution model in SEDFIT (22) using the partial specific volume of *At*-DAPDC and the solvent viscosity and density computed in SEDNTERP (23). Two-dimensional spectrum analyses with 50 Monte Carlo iterations and enhanced van-Holde/Weischet analyses were conducted in UltraScan III (24–26). The data were fitted to a reversible monomer–dimer model with genetic algorithm optimization (27). 96 Monte Carlo iterations were performed in each genetic algorithm fit to determine the 95% confidence intervals for each parameter. During fitting, the monomer molecular mass was fixed at the molecular mass derived from the protein sequence (53.8 kDa for *At*-DAPDC1 and 54.2 kDa for *At*-DAPDC2).

X-ray crystallography

Purified *At*-DAPDC1 and *At*-DAPDC2 were crystallized and X-ray diffraction data collected as reported previously (13). The crystal structures were refined using REFMAC (28) with iterative rounds of model building performed in COOT (29). The structures were deposited in the PDB with accession numbers 6N2A and 6N2F.

Small-angle X-ray scattering

Data were collected at the SAXS/WAXS beamline at the Australian Synchrotron Facility using a 1M Pilatus detector. The two protein samples were injected at 10 mg ml^{-1} into a Superdex 200 PC 3.2/30 gel-filtration column (GE Healthcare) pre-incubated with buffer (20 mM Tris, 100 mM sodium chloride, pH 8.0), before being exposed to the X-ray beam through a 1.5-mm glass capillary at a continuous flow, with 2 s of X-ray exposure per image collected.

Data reduction was performed using CHROMIXS (30), whereas data analysis was performed using the ATSAS software suite (31). Guinier and pairwise distribution analyses were performed using PrimusQT (32), and CRYSOL (33) was used to fit

experimental data with theoretical scattering curves derived from crystallographic models.

Author contributions—J. M. C., M. R. O., R. A. N., K. A. D., A. O. H., M. K., and R. C. D. conceptualization; J. M. C., M. R. O., M. M. L., A. J. B., A. W. W., R. A. N., K. A. D., H. S., and M. K. data curation; J. M. C., M. R. O., M. M. L., A. J. B., M. D. G., H. S., M. K., and R. C. D. formal analysis; J. M. C., M. D. G., and H. S. validation; J. M. C., M. R. O., M. M. L., A. J. B., A. W. W., R. A. N., K. A. D., M. D. G., and M. K. investigation; J. M. C. visualization; J. M. C., M. R. O., M. M. L., A. J. B., A. W. W., R. A. N., K. A. D., and M. K. methodology; J. M. C., P. J. C., and M. R. O. writing-original draft; J .M. C., R. A. N., K. A. D., M. D. G., H. S., A. O. H., M. K., and R. C. D. writing-review and editing; M. D. G. resources; M. D. G., H. S., A. O. H., M. K., and R. C. D. supervision; H. S. software; A. O. H. and R. C. D. funding acquisition; A. O. H. and R. C. D. project administration.

Acknowledgments—We thank Dr. Matthew Perugini from La Trobe University/University of Melbourne for providing the pET16b::ScLys1 plasmid used to facilitate the coupled enzyme kinetic assays. We thank Janet Newman at the C3 Crystallisation Facility (CSIRO, Parkville, Melbourne, Australia) for help with protein crystallization, and the Australian Synchrotron for beamtime (MX2, SAXS) and travel funding. UltraScan analyses of analytical ultracentrifugation data were performed on the UltraScan LIMS cluster at the Bioinformatics Core Facility at the University of Texas Health Science Center at San Antonio and multiple High Performance Computing clusters.

References

1. Bonnett, S. A., Whicher, J. R., Papireddy, K., Florova, G., Smith, J. L., and Reynolds, K. A. (2013) Structural and stereochemical analysis of a modular polyketide synthase ketoreductase domain required for the generation of a cis-alkene. *Chem. Biol.* **20,** 772–783 CrossRef Medline
2. Stavrinides, A., Tatsis, E. C., Caputi, L., Foureau, E., Stevenson, C. E., Lawson, D. M., Courdavault, V., and O'Connor, S. E. (2016) Structural investigation of heteroyohimbine alkaloid synthesis reveals active site elements that control stereoselectivity. *Nat. Commun.* **7,** 12116 CrossRef Medline
3. Dogovski, C., Atkinson, S. C., Dommaraju, S. R., Downton, M., Hor, L., Moore, S., Paxman, J. J., Peverelli, M. G., Qiu, T. W., Reumann, M., Siddiqui, T., Taylor, N. L., Wagner, J., Wubben, J. M., and Perugini, M. A. (2012) in *Enzymology of Bacterial Lysine Biosynthesis* (Ekinci, D., ed) pp. 225–262, InTech, Croatia
4. Born, T. L., and Blanchard, J. S. (1999) Structure/function studies on enzymes in the diaminopimelate pathway of bacterial cell wall biosynthesis. *Curr. Opin. Chem. Biol.* **3,** 607–613 CrossRef Medline
5. Hu, T., Wu, D., Chen, J., Ding, J., Jiang, H., and Shen, X. (2008) The catalytic intermediate stabilized by a "down" active-site loop for diaminopimelate decarboxylase from *Helicobacter pylori*: enzymatic characterization with crystal structure analysis. *J. Biol. Chem.* **283,** 21284–21293 CrossRef Medline
6. Son, H. F., and Kim, K. J. (2018) Structural basis for substrate specificity of meso-diaminopimelic acid decarboxylase from *Corynebacterium glutamicum*. *Biochem. Biophys. Res. Commun.* **495,** 1815–1821 CrossRef Medline
7. Gokulan, K., Rupp, B., Pavelka, M. S., Jr., Jacobs, W. R., Jr., and Sacchettini, J. C. (2003) Crystal structure of *Mycobacterium tuberculosis* diaminopimelate decarboxylase, an essential enzyme in bacterial lysine biosynthesis. *J. Biol. Chem.* **278,** 18588–18596 CrossRef Medline
8. Weyand, S., Kefala, G., Svergun, D. I., and Weiss, M. S. (2009) The three-dimensional structure of diaminopimelate decarboxylase from *Mycobacterium tuberculosis* reveals a tetrameric enzyme organisation. *J. Struct. Funct. Genomics* **10,** 209–217 CrossRef Medline
9. Ray, S. S., Bonanno, J. B., Rajashankar, K. R., Pinho, M. G., He, G., De Lencastre, H., Tomasz, A., and Burley, S. K. (2002) Cocrystal structures of diaminopimelate decarboxylase. *Structure* **10,** 1499–1508 CrossRef Medline
10. Schneider, G., Käck, H., and Lindqvist, Y. (2000) The manifold of vitamin B6 dependent enzymes. *Structure* **8,** R1–R6 CrossRef Medline
11. Peverelli, M. G., Soares da Costa, T. P., Kirby, N., and Perugini, M. A. (2016) Dimerization of bacterial diaminopimelate decarboxylase is essential for catalysis. *J. Biol. Chem.* **291,** 9785–9795 CrossRef Medline
12. Hudson, A. O., Bless, C., Macedo, P., Chatterjee, S. P., Singh, B. K., Gilvarg, C., and Leustek, T. (2005) Biosynthesis of lysine in plants: evidence for a variant of the known bacterial pathways. *Biochim. Biophys. Acta* **1721,** 27–36 CrossRef Medline
13. Oliver, M. R., Crowther, J. M., Leeman, M. M., Kessans, S. A., North, R. A., Donovan, K. A., Griffin, M. D., Suzuki, H., Hudson, A. O., Kasanmascheff, M., and Dobson, R. C. (2014) The purification, crystallization and preliminary X-ray diffraction analysis of two isoforms of meso-diaminopimelate decarboxylase from *Arabidopsis thaliana*. *Acta Crystallogr. F Struct. Biol. Commun.* **70,** 663–668 CrossRef Medline
14. Guzman, L. M., Belin, D., Carson, M. J., and Beckwith, J. (1995) Tight regulation, modulation, and high-level expression by vectors containing the arabinose PBAD promoter. *J. Bacteriol.* **177,** 4121–4130 CrossRef Medline
15. Nachar, V. R., Savka, F. C., McGroty, S. E., Donovan, K. A., North, R. A., Dobson, R. C., Buckley, L. J., and Hudson, A. O. (2012) Genomic and biochemical analysis of the diaminopimelate and lysine biosynthesis pathway in *Verrucomicrobium spinosum*: identification and partial characterization of L,L-diaminopimelate aminotransferase and UDP-*N*-acetylmuramoylalanyl-D-glutamyl-2,6-meso-di. *Front. Microbiol.* **3,** 183 CrossRef Medline
16. Peverelli, M. G., and Perugini, M. A. (2015) An optimized coupled assay for quantifying diaminopimelate decarboxylase activity. *Biochimie* **115,** 78–85 CrossRef Medline
17. Momany, C., Levdikov, V., Blagova, L., and Crews, K. (2002) Crystallization of diaminopimelate decarboxylase from *Escherichia coli*, a stereospecific D-amino-acid decarboxylase. *Acta Crystallogr. D Biol. Crystallogr.* **58,** 549–552 CrossRef Medline
18. Baba, T., Ara, T., Hasegawa, M., Takai, Y., Okumura, Y., Baba, M., Datsenko, K. A., Tomita, M., Wanner, B. L., and Mori, H. (2006) Construction of *Escherichia coli* K-12 in-frame, single-gene knockout mutants: the Keio collection. *Mol. Syst. Biol.* **2,** 2006.0008 CrossRef Medline
19. Gasteiger, E., Hoogland, C., Gattiker, A., Duvaud, S., Wilkins, M. R., Appel, R. D., and Bairoch, A. (2005) *The Proteomics Protocols Handbook* (John, M.W., ed) pp. 571–608, Humana Press, New York
20. Ball, D. W. (2006) *Field Guide to Spectroscopy*, p. 65, SPIE Press, Bellingham, WA
21. Bradford, M. M. (1976) A rapid and sensitive method for the quantitation of microgram quantities of protein utilizing the principle of protein-dye binding. *Anal. Biochem.* **72,** 248–254 CrossRef Medline
22. Schuck, P. (2000) Size-distribution analysis of macromolecules by sedimentation velocity ultracentrifugation and lamm equation modeling. *Biophys. J.* **78,** 1606–1619 Medline
23. Lebowitz, J., Lewis, M. S., and Schuck, P. (2002) Modern analytical ultracentrifugation in protein science: a tutorial review. *Protein Sci.* **11,** 2067–2079 Medline
24. Demeler, B., and Gorbet, G. (2016) *Analytical Ultracentrifugation* (Uchiyama, S., Arisaka, F., Stafford, W., and Laue, T., eds) pp. 119–143, Springer, Tokyo
25. Brookes, E., Cao, W., and Demeler, B. (2010) A two-dimensional spectrum analysis for sedimentation velocity experiments of mixtures with heterogeneity in molecular weight and shape. *Eur. Biophys J.* **39,** 405–414 CrossRef Medline
26. Demeler, B., and van Holde, K. E. (2004) Sedimentation velocity analysis of highly heterogeneous systems. *Anal. Biochem.* **335,** 279–288 CrossRef Medline

27. Demeler, B., Brookes, E., Wang, R., Schirf, V., and Kim, C. A. (2010) Characterization of reversible associations by sedimentation velocity with ultrascan. *Macromol. Biosci.* **10,** 775–782 CrossRef Medline
28. Murshudov, G. N., Vagin, A. A., and Dodson, E. J. (1997) Refinement of macromolecular structures by the maximum-likelihood method. *Acta Crystallogr D Biol Crystallogr.* **53,** 240–255 CrossRef Medline
29. Emsley, P., Lohkamp, B., Scott, W. G., and Cowtan, K. (2010) Features and development of Coot. *Acta Crystallogr. D Biol. Crystallogr.* **66,** 486–501 CrossRef Medline
30. Panjkovich, A., and Svergun, D. I. (2018) CHROMIXS: automatic and interactive analysis of chromatography-coupled small-angle X-ray scattering data. *Bioinformatics* **34,** 1944–1946 CrossRef Medline
31. Petoukhov, M. V., Franke, D., Shkumatov, A. V., Tria, G., Kikhney, A. G., Gajda, M., Gorba, C., Mertens, H. D., Konarev, P. V., and Svergun, D. I. (2012) New developments in the ATSAS program package for small-angle scattering data analysis. *J. Appl. Crystallogr.* **45,** 342–350 CrossRef Medline
32. Konarev, P. V., Volkov, V. V., Sokolova, A. V., Koch, M. H. J., and Svergun, D. I. (2003) PRIMUS: a Windows PC-based system for small-angle scattering data analysis. *J. Appl. Crystallogr.* **36,** 1277–1282 CrossRef
33. Svergun, D., Barberato, C., and Koch, M. H. (1995) CRYSOL–a program to evaluate X-ray solution scattering of biological macromolecules from atomic coordinates. *J. Appl. Crystallogr.* **28,** 768–773 CrossRef